


## Article

# Polarization Analysis of the Impact of Temporal Decorrelation in Synthetic Aperture Radar (SAR) Tomography

Hossein Aghababaei <sup>1,\*</sup> , Giampaolo Ferraioli <sup>2</sup> and Gilda Schirinzi <sup>1</sup> 

<sup>1</sup> Dipartimento di Ingegneria, Università Degli Studi di Napoli “Parthenope”, 80133 Napoli NA, Italy; gilda.schirinzi@uniparthenope.it

<sup>2</sup> Dipartimento di Scienze e Tecnologie, Università Degli Studi di Napoli “Parthenope”, 80133 Napoli NA, Italy; giampaolo.ferraioli@uniparthenope.it

\* Correspondence: aghababaei@uniparthenope.it; Tel.: +39-0815476769

Received: 14 February 2019; Accepted: 18 March 2019; Published: 22 March 2019



**Abstract:** After almost two decades of long investigations into 3D imaging of natural environments, synthetic aperture radar (SAR) tomography (TomoSAR) is now at an operational level. Yet, a major problem that limits the potential of TomoSAR is related to the temporal decorrelation of natural scatterers during multitemporal multibaseline data acquisition. In this paper, a comparative investigation into the effect of temporal decorrelation between employed polarizations is presented. A particular focus is put on practical and statistical analysis of the dispersion of polarimetric vertical reflectivity in the presence of temporal decorrelation. The analysis is based on the synthesis of all feasible polarimetric responses of a given scatterer from its measurements of a linear orthonormal basis. Such an analysis offers a comprehension of the expected level of temporal decorrelation in TomoSAR focusing with respect to employed polarization. The analysis was performed by simulating temporal decorrelation with different terms, depending on the vertical structure and polarization, which are important aspects in a forest scenario. Moreover, the experiment was extended to a P-band dataset relative to the forest site of Remningstorp, Sweden, which was acquired through the German Aerospace Center’s experimental SAR (E-SAR) airborne system in the framework of the European Space Agency (ESA) campaign BioSAR.

**Keywords:** TomoSAR; temporal decorrelation; polarization synthesizing

## 1. Introduction

Synthetic aperture radar (SAR) tomography (TomoSAR) with resolution capabilities in the height dimension is today well assessed and widely exploited in remote sensing of complex scenarios, such as agricultural and forested areas [1–4]. Today, two main spaceborne missions, NASA-Indian space research organization (NISAR) [5] and Tandem-L [6], are under development, with the goal of forest structure monitoring and biomass mapping using SAR tomography.

Adapted TomoSAR focusing techniques are mainly based on array processing of multibaseline (MB) repeat-pass radar data. Given multitemporal MB data, the accuracy and potential of TomoSAR can be limited by temporal coherence loss of natural scatterers due to their geometrical and dielectric changes in the interferometric time interval. In this case, possible effects ranging from blurring to defocusing can arise in the temporal synthesis of the elevation array [7,8]. In the literature, the defocusing issue has been mitigated by employing a distributed source model in the domain of temporal frequency [7,8]. However, whatever the processing technique is, temporal decorrelation is a critical issue for the feasibility of SAR tomography in a volumetric scenario. Generally, in forest and

agricultural areas, temporal decorrelation may occur at timescales ranging from a fraction of a second to years. The occurrence of temporal decorrelation in that timescale constitutes a particular criticality in the development of spaceborne missions for forest tomography. As has been noted in Reference [9] and in particular with regard to biomass mapping, a temporal decorrelation effect appears to be a critical factor at even a mild temporal baseline (17 days). Therefore, with the aim of a reliable result in multitemporal data processing, the physics behind temporal decorrelation should be perceived.

Temporal decorrelation may arise from different sources, including biological growth or weather conditions. Their effects on multitemporal SAR data may impair only the magnitude of the coherence without a direct effect on the phase, such as motion induced by wind, or change the dielectric properties of the scatterers with a more direct effect on the phase, such as that induced by rain [10]. Temporal decorrelation may be modeled by some analytical formulations. In practice, its effect on the observed interferometric coherence is complicated. However, commonly simple yet reliable representative real valued exponential models are available in the literature to model wind-induced and biological growth decorrelation. Such models have already been extended to Brownian motion [11] and birth-and-death processes [12]. Having a reliable model supports the interpretation of interferometric coherence and allows for comprehension of the possible effect of temporal decorrelation on the reconstructed elevation array.

In general, the mechanism of temporal decorrelation is very complex and beyond the influence of scene characteristics (e.g., land use, soil moisture): A dependence of temporal decorrelation on acquisition parameters in terms of frequency, temporal baseline, resolution, and polarization is expected [13]. Yet, assessments and comprehension of the expected levels of temporal decorrelation are required to aim for optimal data selection for feasible TomoSAR applications in natural scenarios. In the literature regarding multitemporal MB SAR data, some studies have been dedicated to analyzing the effects of temporal decorrelation with respect to the employed frequency of the data [13–15], and as evidenced by the literature, longer wavelengths have demonstrated more robustness and less sensitivity to temporal decorrelation. However, beyond some practical reports on coherence loss, practically no effort has been dedicated to the assessment of temporal decorrelation with respect to the polarization employed in TomoSAR.

Bearing in mind these key points, in order to provide instruments for a more robust reconstruction in SAR tomography and to improve the understanding of temporal decorrelation effects, in this paper a comparative analysis on the effect of temporal decorrelation with respect to polarization is presented. The analysis is based on the dispersion of the reflectivity profile in all synthesized polarizations obtained from polarimetric measurements in a linear orthonormal basis. The most important consequence of the polarization synthesis process was the full characterization of the scatterer under temporal decorrelation, allowing for better identification of the optimal polarization for tomographic processing algorithms. This will pave the way for comprehension of the expected effects of temporal decorrelation in TomoSAR focusing with respect to the employed polarization, complementing frequency-oriented studies.

The paper begins with an overview on the polarimetric SAR signal model as well as the basic principles of TomoSAR focusing in Section 2. An introduction to polarization synthesis theory, in particular the case of MB data, is given in Section 3. A realistic simulation process for temporal decorrelation, including different terms with a peculiar dependence on vertical structure and polarization, is reported in Section 4. Comparative analyses on the effect of temporal decorrelation between employed polarizations with reference to the dispersion of reconstructed reflectivity using simulated and real data acquired by the European Space Agency's campaign BIOSAR are provided in Section 5. Further discussions and conclusions on the results reported by the analyses are then given in Sections 6 and 7.

## 2. Polarimetric SAR Signal Model

Let us refer to a stack of  $N$  azimuth-range focused polarimetric SAR images obtained by a repeat-pass sensor, coregistered, deramped, and phase-compensated with respect to a given master image. For each pixel, the vector collecting the  $N$  images is modeled as a superposition of the contributions from all scatterers lying in the considered cell, each at different heights [16]. From this fact and in the case of fully polarimetric MB data, the polarimetric MB target vector  $\mathbf{x}$ , in lexicographic representation, can be presented as

$$\mathbf{x} = \frac{1}{2} [\mathbf{x}_{hh}^T \sqrt{2} \mathbf{x}_{hv}^T \mathbf{x}_{vv}^T]^T = \sum_z \gamma_p(z) \odot \mathbf{b}(z) + \mathbf{w}, \quad (1)$$

where  $\mathbf{x}$  is a  $3N \times 1$  vector composed of three  $N \times 1$  MB complex vectors in conventional linear polarizations ( $hh$ ,  $hv$ , and  $vv$ ; see the next section);  $\odot$  represents the Hadamard product;  $^T$  indicates the transpose operator;  $\mathbf{b}(z) = [k_1 \mathbf{a}(z)^T \ k_2 \mathbf{a}(z)^T \ k_3 \mathbf{a}(z)^T]^T$ , in which  $\mathbf{a}(z)$  is the steering vector,  $\mathbf{k} = [k_1, k_2, k_3]$  is a unitary reflection mechanism, and  $\mathbf{k}^\dagger \mathbf{k} = 1$ ; and  $\mathbf{w}$  denotes the additive noise. Moreover,  $\gamma_p(z)$  is the complex polarimetric reflectivity at a height of  $z$ , which corresponds to the span in the polarimetric SAR literature.

In a natural environment with distributed scatterers, where the interference of scatterers in a cell leads to a speckle phenomenon, a second-order statistical framework is commonly adapted. In this case, polarimetric TomoSAR aims to estimate the polarimetric backscattering power or reflectivity  $|\gamma_p(z)|^2$  using the sample polarimetric covariance matrix of MB data (i.e.,  $\hat{\mathbf{C}} = \sum_k^K \mathbf{x}(k) \mathbf{x}(k)^\dagger / K$ ) estimated over the  $K$  spatial neighborhood of the pixel of interest, where  $^\dagger$  denotes the Hermitian operator. Many array processing techniques can be employed for the reconstruction of backscattering power. Among these, the adaptive polarimetric Capon introduced in References [17,18], which has a high side-lobe suppressing capability, is a typical technique in polarimetric TomoSAR reconstruction, in which the estimated polarimetric reflectivity is given by

$$P(z) = \frac{1}{d_{\min}(\mathbf{b}(z, \mathbf{k})^\dagger \hat{\mathbf{C}}^{-1} \mathbf{b}(z, \mathbf{k}))}, \quad (2)$$

where  $\mathbf{b}(z, \mathbf{k}) = \mathbf{k} \otimes \mathbf{a}(z)$ ,  $\otimes$  denotes the Kronecker product, and  $d_{\min}(\cdot)$  is the minimum eigenvalue operator.

In repeat-pass interferometric image acquisition, the presence of temporal decorrelation is equivalent to the variation of reflectivity distribution over the acquisition times in Equation (1), which leads to defocusing, blurring in the reconstruction of the elevation array, and some uncertainties in the parameter estimation as well [8]. In the next sections, this problem will be investigated and taken into account.

## 3. Multibaseline Polarization Synthesizing Theory

Typically, fully polarimetric radar systems measure complex backscattering of a target on a linear horizontal ( $h$ ) and vertical ( $v$ ) orthogonal polarization basis  $\{h, v\}$ . Hence, the response from a reciprocal medium can be represented by a vector that has three unique elements  $\mathbf{v}_{\{h,v\}} = [x_{hh} \ x_{hv} \ x_{vv}]^T$ , where  $x_{hv}$  is the complex backscattering from the vertical polarized transmitted signal and the horizontal polarized return. However, due to the fact that any orthogonal set of elliptically polarized states can form a polarization basis, then the polarimetric response vector can be represented in any desired orthogonal elliptical basis  $\{p, q\}$ , in which  $q$  is an orthogonal complement of  $p$  [19]. The theory of polarization synthesis [19] provides an efficient way to fully characterize the polarimetric response of the target.

Alternatively, the polarization state of an electromagnetic wave can be characterized by the complex polarization ratio  $\rho$  represents in terms of geometrical parameters [20]:

$$\rho = \frac{\cos(2\chi) \sin(2\phi) + i \sin(2\chi)}{1 + \cos(2\chi) \cos(2\phi)}, \quad (3)$$

where  $\chi$  and  $\phi$  are the ellipticity and orientation angles within ranges of  $[-45, 45]$  and  $[0, 180]$  degrees, respectively. From Equation (3), the polarimetric response vector from the linear basis  $\{h, v\}$  can be transformed into a desired  $\{p, q\}$  basis with a specific orientation and ellipticity  $\phi$  and  $\chi$  as

$$\mathbf{v}_{\{p,q\}} = \underbrace{\frac{1}{1 + \rho\rho^\dagger} \begin{bmatrix} 1 & \sqrt{2}\rho & \rho^2 \\ -\sqrt{2}\rho^\dagger & 1 - \rho\rho^\dagger & \sqrt{2}\rho \\ \rho^{\dagger 2} & -\sqrt{2}\rho^\dagger & 1 \end{bmatrix}}_{\mathbf{U}} \mathbf{v}_{\{h,v\}}. \quad (4)$$

From Equation (4), the polarization synthesis theory can be extended to the case of an MB dataset. Hence, the defined lexicographic target vector  $\mathbf{x}$  in Equation (1) and its corresponding covariance matrix  $\hat{\mathbf{C}}$  in a desired polarization basis  $\{p, q\}$  with an orientation and ellipticity of  $\phi$  and  $\chi$ , respectively, are represented by

$$\begin{aligned} \mathbf{x}_{\{p,q\}} &= \frac{1}{2} [\mathbf{x}_{pp}^T \sqrt{2} \mathbf{x}_{pq}^T \mathbf{x}_{qq}^T]^T = \mathbf{A} \mathbf{x} \\ \hat{\mathbf{C}}_{\{p,q\}} &= \mathbf{A}_{\{\phi,\chi\}} \hat{\mathbf{C}}_{\{h,v\}} \mathbf{A}_{\{\phi,\chi\}}^\dagger \end{aligned} \quad (5)$$

In Equation (5), the unitary transformation matrix is given by  $\mathbf{A}_{\{\phi,\chi\}} = \mathbf{U} \otimes \mathbf{I}$ , where  $\mathbf{I}$  is the  $N \times N$  identity matrix, and  $\mathbf{U}$  is defined in Equation (4).

### 3.1. TomoSAR Reflectivity Cube

From the derivation of the polarimetric covariance matrix in any desired polarization basis  $\hat{\mathbf{C}}_{\{p,q\}}$ , the polarimetric reflectivity can be reconstructed for each possible basis as

$$P(\phi, \chi, z) = \frac{1}{d_{\min}(\mathbf{b}(z, \mathbf{k})^\dagger (\mathbf{A}_{\{\phi,\chi\}} \hat{\mathbf{C}}_{\{h,v\}} \mathbf{A}_{\{\phi,\chi\}}^\dagger)^{-1} \mathbf{b}(z, \mathbf{k}))}. \quad (6)$$

In this paper, in order to fully evaluate the effect of temporal decorrelation in polarimetric TomoSAR reconstruction, the estimation of the polarimetric covariance matrix was extended to all possible bases, where the bases are defined by the variation of geometrical parameters  $\chi$  and  $\phi$  in their specified ranges with increments of one degree. Hence, for a selected pixel, reconstruction with different bases resulted in the generation of TomoSAR reflectivity cubes estimated using Equation (6), where the columns of the cube are the reflectivity profiles associated with the specific polarization basis defined by  $(\phi, \chi)$ .

### 3.2. Dispersion Analysis

A straightforward way of analyzing the impact of temporal decorrelation in TomoSAR focusing is to measure the dispersion of the reflectivity profile. Generally, as a matter of fact, reconstructed blurred or defocused reflectivity due to temporal decorrelation appears with lower sharpness [21]. In information theory, the sharpness can be measured by contrast defined as  $\text{cnt} = \Sigma(P(z) - \mu_P) / (\mu_P M)$ , where  $P(z)$  is the reconstructed vertical reflectivity profile at a height of  $z$ , and  $\mu_P$  and  $M$  are the mean and the length of the reflectivity vector, respectively. Hence, contrast can be a proper indicator of the temporal decorrelation effect and dispersion of the signal. It is needless to point out that the higher the effect of temporal decorrelation, the lower the contrast of the reconstructed reflectivity profile.

From the computation of contrast for the reflectivity profiles in all polarization bases, a 3D view can be presented of the focusing quality in any polarization basis. In the plot, the two horizontal dimensions correspond to geometrical parameters  $\chi$  and  $\phi$ , while the third one is related to the contrast of the reconstructed vertical polarimetric reflectivity. As an example, Figure 1 shows a 3D-view plot of a sample forest pixel with ground and canopy backscattering contributions. For the considered forest



pixel, MB data were obtained in the absence of temporal decorrelation (see the details in Section 4). Simply, the following steps were followed in the generation of such a plot:

- (1) Estimate the sample covariance matrix  $\hat{\mathbf{C}}$  in the measurement polarization basis of radar, i.e.,  $\{h, v\}$ , a Cartesian polarization basis;
- (2) Reconstruct the reflectivity  $\mathbf{P}$  of each polarization basis using Equation (6), where the bases are generated by varying  $\chi$  and  $\phi$  in their specified range with increments of 1 degree;
- (3) Estimate the contrast of the recovered reflectivity profiles in each basis.

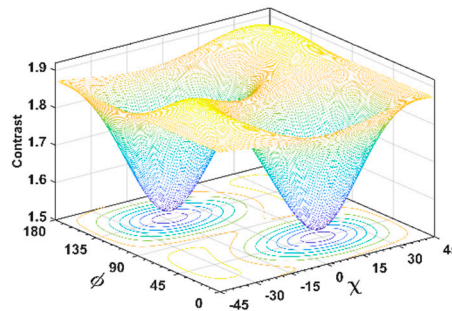


**Figure 1.** A 3D view of the focusing capability of a reconstructed vertical profile in different polarization bases.

Apparently, the dispersion of the reflectivity profile in any desired polarization basis can be represented by a contrast deviation between the profiles obtained in the absence and presence of temporal decorrelation. Accordingly, a comparison of two 3D-view plots of contrast, one related to original data in the absence of temporal decorrelation and the other one related to a temporally decorrelated MB dataset, showed the dispersion of the reflectivity obtained in each polarization basis due to temporal decorrelation. Subsequently, the proposed framework of this study was laid out, a comparison of two 3D plots of the contrast obtained from two MB datasets related to a specific resolution cell, one stack obtained in the zero-temporal baseline and the other affected by some temporal decorrelation.

It should be noted that the graph of Figure 1 was considered to be a reference, or temporal decorrelation-free stack, in the simulation process. More details will be provided in the next sections.

#### 4. Numerical Examples

With the aim of comparative analysis on the effect of temporal decorrelation with respect to polarization, in the following subsections, polarimetric MB data related to a forest area are simulated in the absence and presence of temporal decorrelation. The simulation process is described in Section 4.1, while analyses are reported in Section 4.2. The outcomes of the performed analyses are representations of the temporal decorrelation effect in different polarization bases by comparing 3D contrast plots obtained from error-free data and temporal decorrelation-affected data.

##### 4.1. Multitemporal MB Data Simulation

Natural environments are usually affected by temporal decorrelation. In particular, wind-induced temporal decorrelation and biological growth are the main sources of temporal decorrelation in forested areas, where dependence on the vertical structure of the forest and on the polarization of the image is inevitable [22]. In principle, a SAR image in any specific polarization corresponds to the superposition of all backscatterings lying in the same azimuth-range resolution cell but having different elevations, i.e.,  $\sum_z(\gamma(z)\mathbf{a}(z))$ . In forest realities and due to temporal decorrelation, complex backscattering  $\gamma(z)$  changes over the acquisition time, i.e.,  $\gamma(z) = [\gamma(z, t_1), \gamma(z, t_2), \dots, \gamma(z, t_N)]$ . In fact, such a temporal variation of scatterers can be characterized by being aware of the model of temporal decorrelation.

Considering wind and vegetation growth effects (as short and long terms), the exponential model of temporal decorrelation observed in multitemporal coherence  $C_T = E\{\gamma(z)\gamma(z)^\dagger\}$  can be written as [10]

$$C_T(r, s) = \begin{cases} \frac{1}{1+\mu} \exp(-\frac{|t_s-t_r|}{\tau_v}) \exp(-\frac{1}{2}(\frac{4\pi}{\lambda}\sigma_v)^2) + \frac{\mu}{1+\mu} \exp(-\frac{|t_s-t_r|}{\tau_g}) & , t_s \neq t_r \\ 1 & , t_s = t_r \end{cases}, \quad (7)$$

where  $t_s$  and  $t_r$  indicate  $s$ th and  $r$ th temporal baselines;  $\lambda$  is the wavelength;  $\tau_v$  and  $\tau_g$  are the decorrelation time constants for canopy and ground, respectively;  $\sigma_v$  is the motion standard deviation in the canopy; and finally,  $\mu$  is the ground-to-volume ratio that is dependent on polarization.

In order to simulate multitemporal data affected by temporal decorrelation, a two-component complex vertical reflectivity signal  $\gamma$  in three linear polarizations ( $hh$ ,  $hv$ , and  $vv$ ) was simulated. The complex signal had two backscattering phase centers, one on the ground with zero angular spreading and the other situated 15 m above the ground scatterer with nonzero bandwidth. The polarimetric scattering matrix of the canopy was set to the model of the volumetric scattering mechanism given as an ensemble of rotated vertical thin cylinders in Reference [23], while that of the ground was set to the double bounce scattering mechanism [23]. In order to create a multitemporal complex backscattering signal  $\{\gamma(t_1), \gamma(t_2), \dots, \gamma(t_N)\}$  for each polarization, first the coherence matrix of complex reflectivity at the ground and canopy height levels was computed as

$$\begin{aligned} C_{T\_canopy}(r, s) &= \begin{cases} \frac{|\gamma_{zv}|^2}{1+\mu} \exp(-\frac{|t_s-t_r|}{\tau_v}) \exp(-\frac{1}{2}(\frac{4\pi}{\lambda}\sigma_v)^2) & , t_s \neq t_r \\ 1 & , t_s = t_r \end{cases} \\ C_{T\_ground}(r, s) &= \begin{cases} |\gamma_{zg}|^2 \frac{\mu}{1+\mu} \exp(-\frac{|t_s-t_r|}{\tau_g}) & , t_s \neq t_r \\ 1 & , t_s = t_r \end{cases} \end{aligned}, \quad (8)$$

where  $|\gamma_{zg}|$  and  $|\gamma_{zv}|$  are backscattering powers at the ground and canopy height levels at a specific polarization. Then, by multiplying a random complex vector by the square root of the coherence matrix at each ground and canopy height level in Equation (8), the multitemporal complex backscattering signal  $\{\gamma(t_1), \gamma(t_2), \dots, \gamma(t_N)\}$  can be obtained. Finally, from the complex reflectivity at each time and using the coherent superposition of ground and canopy scatterers, multitemporal data can be generated.

In accordance with the above-described way of simulating, three different stacks of polarimetric MB data were simulated to correspond to (1) temporal decorrelation-free, (2) mild, and (3) strong temporal decorrelation scenarios. Each simulated stack consisted of  $N = 6$  images acquired by P-band sensor and vertically oriented tracks, where the baselines were evenly distributed and spanned a spatial synthetic of 75 m (see Table 1 for details of baseline information). Moreover, we note that the ground-to-volume ratio was set to 5, 2.5, and 4 dB in the  $hh$ ,  $hv$ , and  $vv$  polarizations, respectively. Furthermore, the overall temporal baseline was set to 2.25 months, with specified spans of 2.25, 1.35, 1.80, 0.90, and 0.45 months as the reference time (Table 1).

**Table 1.** The baseline information of the simulated dataset.

Image Number	1	2	3	4	5	6
Spatial baseline (m)	0	15	30	45	60	75
Temporal baseline (months)	0	2.25	1.35	1.80	0.90	0.45

#### 4.2. Results from Simulated Data

First, the simulated polarimetric MB data in the absence of temporal decorrelation when the parameters of decorrelation were set to zero were considered. For this simulated fully polarimetric MB data, and from the variation of the geometrical parameters ( $\chi, \phi$ ), the polarimetric reflectivity in different polarization bases was reconstructed using Equation (6). Figure 1 shows contrasts of

polarimetric reflectivity in a 3D view for this simulated polarimetric two-component signal. As can be seen, better-focused vertical reflectivity profiles were obtained in the circular ( $\chi = \pm 45^\circ$ ) and horizontal-orientated polarizations ( $\phi = 0$  or  $180^\circ$ ) characterized by higher values of contrast.

To provide an answer to the question of which polarization basis was more robust with respect to temporal decorrelation effects, we effected a mild temporal decorrelation on the simulated two-component signal, where the parameters of temporal decorrelation were set to  $\sigma_v = 0.02$ ,  $\tau_g = 12.5$ ,  $\tau_v = 8$ . In a way similar to the generation of Figure 1, for the simulated multitemporal data affected by mild temporal decorrelation, a polarimetric reflectivity cube using Equation (6) was computed, and a 3D contrast view is presented in Figure 2a. As can be expected and in comparison to Figure 1, the contrast was substantially decreased with multitemporal data affected by mild temporal decorrelation.

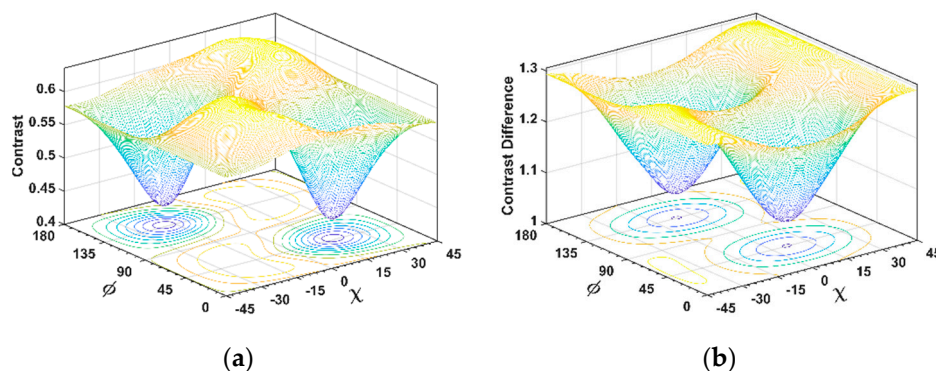


**Figure 2.** Mild temporal decorrelation-affected data: (a) A 3D view plot of polarimetric synthetic aperture radar (SAR) tomography (TomoSAR) focusing capability; (b) polarization TomoSAR dispersion obtained by subtracting Figure 2a from Figure 1.

Having the polarimetric reflectivity in the absence (Figure 1) and presence of temporal decorrelation (Figure 2a) allowed for an estimation of the dispersion on the reconstructed reflectivity due to temporal decorrelation. A 3D view of the temporal decorrelation dispersion of the above-mentioned scenario is provided in Figure 2b by subtracting the contrast between the original simulated signal (Figure 1) and the temporally affected one (Figure 2a). It is basically understandable that the difference in contrast values between the original and temporally affected signals were due to temporal decorrelation, where the higher the contrast difference, the higher the effect of temporal decorrelation. Hence, the contrast difference in all of the polarization bases could be considered to be a polarization dispersion measure of temporal decorrelation. From the polarization TomoSAR dispersion 3D view in Figure 2b, it could be confirmed that regardless of the focusing capability, the circular polarization bases were mostly affected by temporal decorrelation. Instead, two polarization bases, indicated by the cavities in the given 3D plot, showed more robustness to temporal decorrelation. The characterized geometrical parameters of these bases were ( $\chi = -5^\circ$ ,  $\phi = 135^\circ$ ) and ( $\chi = 6^\circ$ ,  $\phi = 45^\circ$ ), indicating shrunken elliptical polarization bases with orientations of  $45^\circ$  and  $135^\circ$ . Furthermore, it could be verified that the standard horizontal–vertical linear polarization basis ( $\chi = 0$ ,  $\phi = 0^\circ$ ) was more sensitive to the decorrelation effect in comparison to the optimal founded bases.

In addition, the experiment was extended to another simulation case by increasing the level of temporal decorrelation ( $\sigma_v = 0.08$ ,  $\tau_g = 6.5$ ,  $\tau_v = 4$ ). In this case, similar results were also reported (see Figure 3). However, the standard deviation of the polarization TomoSAR dispersion (Figure 3b) increased due to the decrease in the contrasts of the reflectivity in the multitemporal data affected by strong temporal decorrelation. Nevertheless, it could be verified that in this case also, the left- and right-handed circular bases were more sensitive to the decorrelation effect, while it was still possible to observe two main polarization bases ( $\chi = 5^\circ$ ,  $\phi = 55^\circ$ ) and ( $\chi = -8^\circ$ ,  $\phi = 135^\circ$ ) with high robustness to the temporal decorrelation effect.

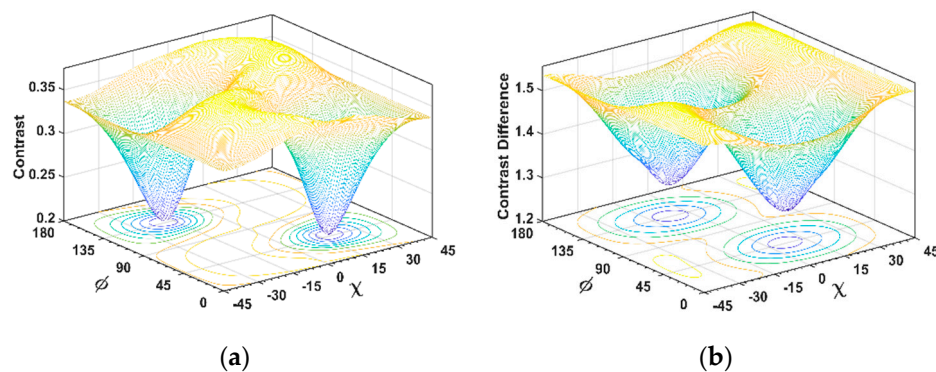


**Figure 3.** Strong temporal decorrelation-affected data: (a) A 3D view plot of polarimetric TomoSAR focusing capability; (b) polarization TomoSAR dispersion obtained by subtracting Figure 3a from Figure 1.

## 5. Experimental Results

The European Space Agency (ESA) campaign BIOSAR 2007 has been aimed at providing a dataset for the study of long-term missions of biomass mapping [24]. In this framework,  $N = 9$  fully polarimetric images of the forest site of Remningstorp, Sweden, were considered. In the study area, the terrain topography is fairly flat, and the tree heights are on the order of 20 m, with peaks up to 30 m. The horizontal baseline spacing is around 10 m, resulting in a Fourier resolution of approximately 27.5 m in the elevation direction (mid-range). Moreover, the images were acquired for three time periods: 9 March 2007, 2 April 2007, and 2 May 2007. Such an overall time span would correspond to a mild or even strong temporal decorrelation scenario. Figure 4 shows a polarimetric master image in a Pauli color composite, and Table 2 presents baseline configurations.

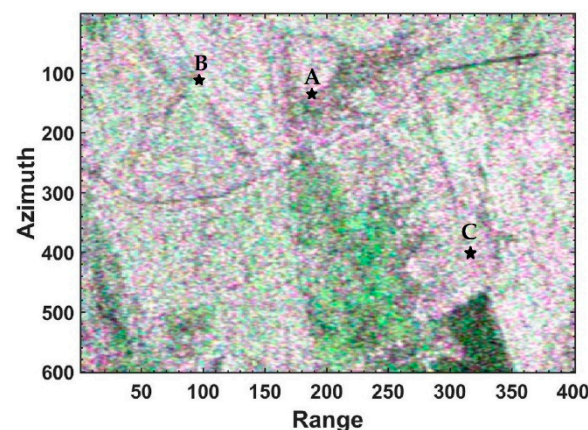


**Figure 4.** Pauli color composite of a master image of BioSAR data. Points (A, B, C) are analyzed cells in the polarization synthesis.

**Table 2.** The baseline information of the BioSAR dataset.

Image Number	1	2	3	4	5	6	7	8	9
Acquisitions date	2 May	2 May	2 May	2 May	2 April	2 April	2 April	9 March	9 March
Spatial baseline (m)	0	10	80	30	40	50	20	60	70
Temporal baseline (days)	0	0	0	0	30	30	56	56	56

### 5.1. Generation of Decorrelation-Free and Decorrelation-Affected Data Stacks

The quantification of the polarization TomoSAR dispersion of the signal using a real dataset and in the absence of the original data (without temporal decorrelation) was a problematic task. In order to analyze the temporal decorrelation effect using the BioSAR data, similarly to the case of the numerical



experiment, two MB data stacks were required, one related to a decorrelation-free and the other related to a temporal decorrelation-affected scenario. The whole stack of BioSAR data (nine images), with a temporal baseline of approximately 2 months, generated a temporal decorrelation-affected stack, while in order to build a stack of decorrelation-free data, a specific framework was needed, explained as follows.

A particular temporal baseline configuration of the BioSAR data (see Table 2) could bring a possibility of reconstructing quasi-error-free reflectivity without a temporal decorrelation effect. With this aim, an MB stack of the first four images obtained on the same day (2 May) was generated. This stack was considered to be a decorrelation-free stack, while all nine images together, as mentioned before, generated a decorrelation-affected stack. Basically, the reconstructed polarimetric reflectivity of the first four images was free of a temporal decorrelation effect. However, it could not be used as a reference signal to compare its quality to the reflectivity obtained from the nine-data case. Evidently, this was due to the fact that in some resolution cells, by increasing the number of baselines, a better-focused signal could be obtained using a nine-image stack in comparison to a stack of four images. Hence, with the aim of fair comparison and as an example, three points were selected by evaluating the ensemble coherence and the contrast of the reconstructed profiles. The locations of the selected cells are shown in Figure 4. All of the points were selected in such a way that the contrast of the focused polarimetric reflectivity from the case of four images outperformed that obtained by all nine images (see Table 3 and Figure 5).

**Table 3.** Focusing quantification of the three points illustrated in Figure 4.

	Point A	Point B	Point C
Ensemble coherence	0.96	0.94	0.90
Contrast from four baselines	1.41	1.57	1.86
Contrast from nine baselines	1.41	1.06	0.77

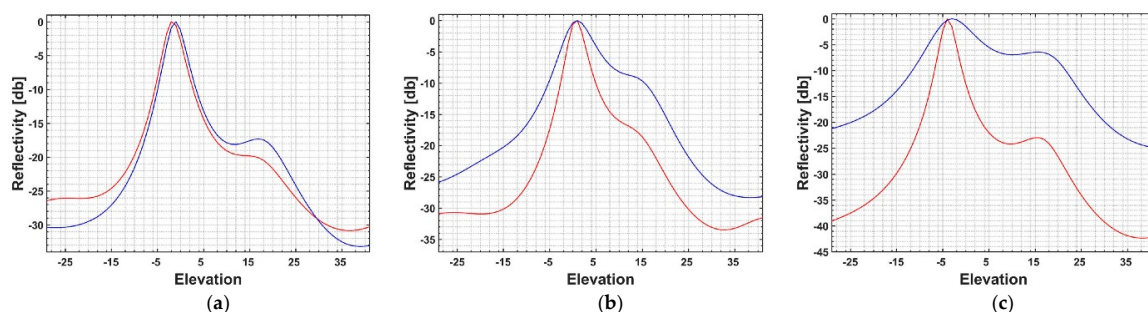


**Figure 5.** The polarimetric reflectivity of the three selected cells in Figure 4, with 4 (red) and 9 (blue) data stacks: (a) point A, (b) point B, (c) point C.

It should be noted that the ensemble coherence for each pixel from the MB fully polarimetric data set was computed as

$$\text{coherence} = \max_z \frac{1}{PN} \left| \sum_{p=1}^P \sum_{n=1}^N \exp(i\varphi_{p,n}) \text{conj}(a_n(z)) \right|, \quad (9)$$

where  $\varphi_{p,n}$  is a phase of a selected pixel in the  $p$ th polarization state with the specifications of the same transit-receive wave polarization of the  $n$ th image;  $a_n(z)$  is the  $n$ th element of the steering vector; and  $\text{conj}(\cdot)$  indicates a conjugate operator. The parameter  $p$  indicates the number of polarizations  $p = 3$ , and  $N$  indicates the number of baselines, i.e.,  $N = 4$ , and 9.

From the given reflectivity profiles (Figure 5) using the two data stacks, it could be noticed that for all the considered cells, reconstruction using the four-data stack (red profiles) as the decorrelation-free profiles outperformed that obtained from the nine-data stack, which was affected by temporal

decorrelation (blue profiles). Hence, under such a condition, the first four images were considered to be a reference and a decorrelation-free data stack in evaluating the temporal decorrelation effect presented in the stack of nine images.

## 5.2. Analysis of Temporal Decorrelation

For the three selected points shown in Figure 4, two stacks of MB datasets (four and nine images) were generated, and consequently, through using Equation (6) and after computing the contrasts of the reconstructed reflectivity profiles, the plots of the contrast 3D view were generated. Figures 6–8 show 3D views of the focusing capability of polarimetric TomoSAR in different polarization bases for the selected points. In these figures, the left plots (Figures 6a, 7a and 8a) are related to the temporal decorrelation-free dataset (four images), while the middle ones (Figures 6b, 7b and 8b) are associated with the case of the nine-dataset. Through having the focusing measures of the error-free and temporal decorrelated data and subtracting them from each other, a TomoSAR dispersion 3D view could be provided in the right plots of Figures 6c, 7c and 8c.

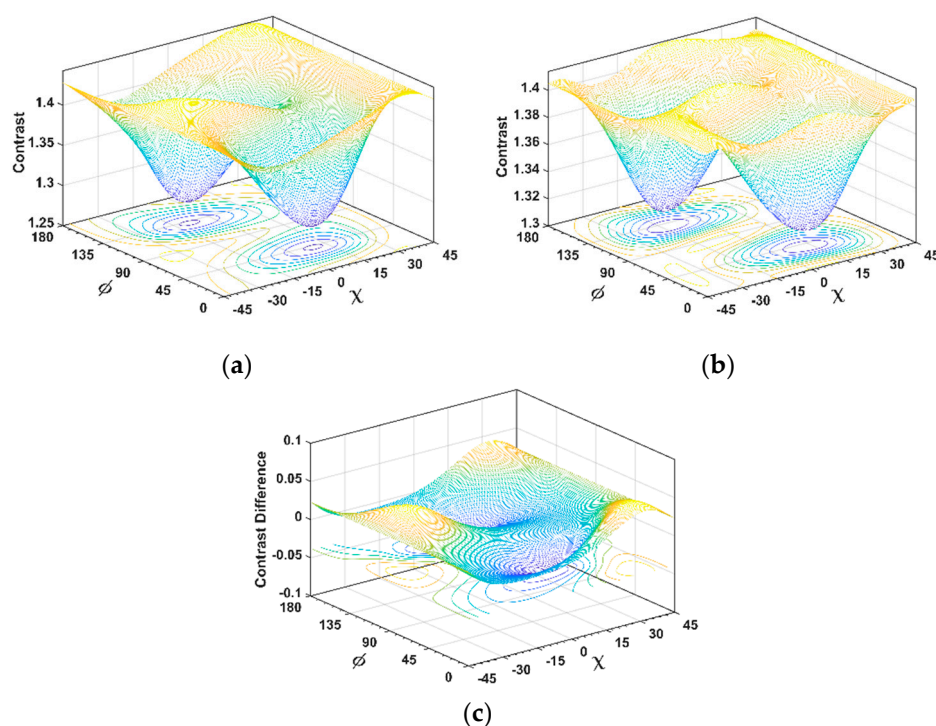


**Figure 6.** Polarimetric TomoSAR focusing capability for cell A: (a) Four-data stack, (b) nine-data stack, (c) polarization TomoSAR dispersion obtained through the subtraction of (b) from (a).

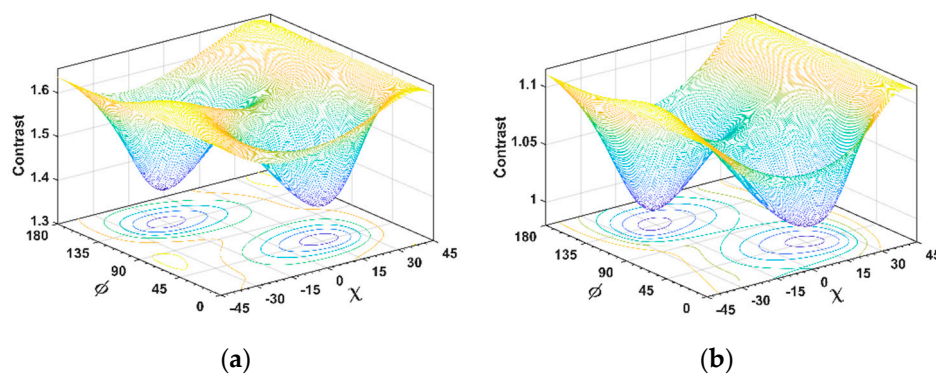


**Figure 7.** Cont.



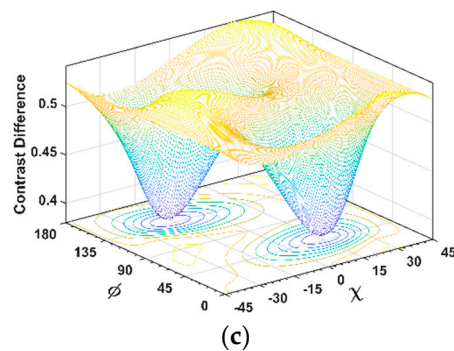


**Figure 7.** Polarimetric TomoSAR focusing capability for cell B: (a) Four-data stack, (b) nine-data stack, (c) polarization TomoSAR dispersion obtained through the subtraction of (b) from (a).

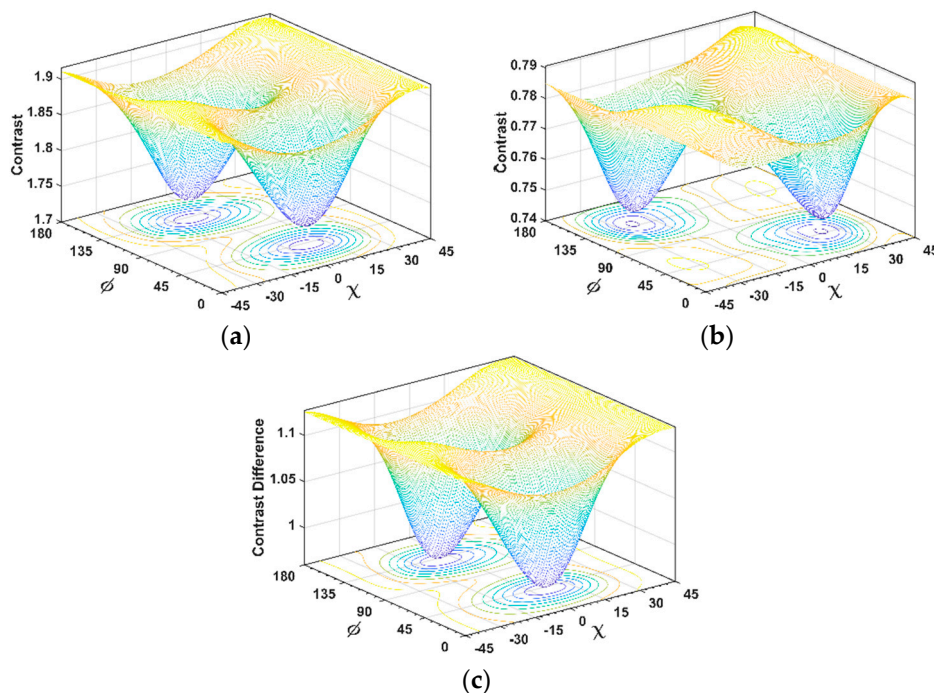


**Figure 8.** Polarimetric TomoSAR focusing capability for cell C: (a) Four-data stack, (b) nine-data stack, (c) polarization TomoSAR dispersion obtained through the subtraction of (b) from (a).

Moreover, in order to extend the analysis, all of the pixels of Figure 4 that satisfied the above-described condition in Section 5.1 were discovered. Then, through the generation of the two MB stacks for those pixels, and after an analysis of the reconstructed polarization TomoSAR dispersion, the histograms of the most robust polarizations in terms of geometrical parameters were reported (in Figures 9 and 10).

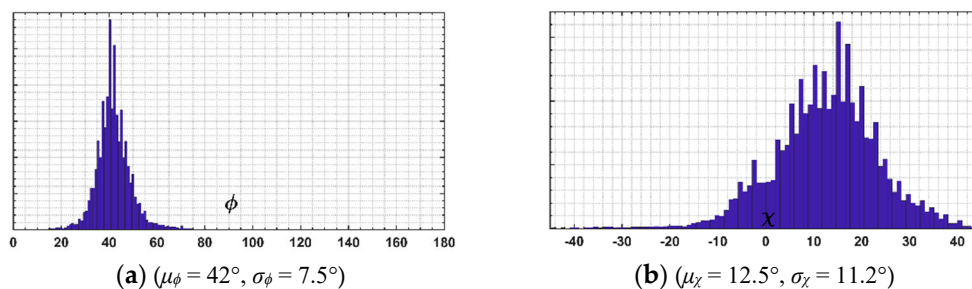


**Figure 9.** Histograms of the most robust polarizations, extracted from the first cavity: (a) Orientation angle and (b) ellipticity.

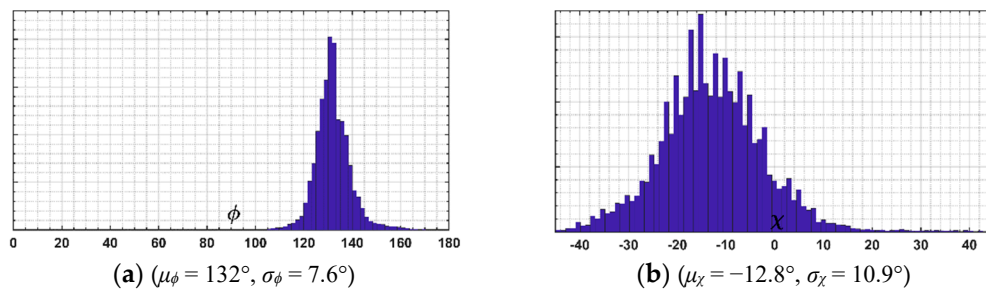


**Figure 10.** Histograms of the most robust polarizations, extracted from the second cavity: (a) Orientation angle and (b) ellipticity.

## 6. Discussion

From the assessed experiments and analyses, it is possible to characterize polarization behavior with respect to the effect of temporal decorrelation. From the experimental results in the previous section, we can observe that from point A to C, the effect of temporal decorrelation increased with decreases in the coherence and contrast (see Table 2). This can also be noticed from the given reflectivity profiles (Figure 5) using the two data stacks, where the case of the four-data stack (the decorrelation-free profiles) outperformed the ones obtained from the “nine” images affected by temporal decorrelation.

Due to a high value of coherence and the same contrast of reflectivity, it could be declared that the effect of temporal decorrelation for the selected point A was minimal. Thus, it was expected to have zero dispersion in a comparison of reflectivity from the two considered stacks. For this point, very similar plots for the “four” and “nine” datasets were obtained (Figure 6a,b), where the computed polarization TomoSAR dispersion had a standard deviation of 0.03 around zero dispersion (Figure 6c). Such a dispersion verified that the reconstructed decorrelation-free profile from the four-data stack could be considered to be a quasi-error-free profile, with the condition of having upper or equal contrast and coherence with the nine-data case.

For point B, the estimated polarization TomoSAR dispersion is presented in Figure 7c. In an analogy to the simulated data, the standard deviation of the contrast for the temporally decorrelated data (nine-data stack, Figure 7b) was reduced with respect to the error-free one (four-data stack, Figure 7a). Moreover, from Figure 7c, more sensitivity of the circular polarization bases to temporal decorrelation could be verified, while the two cavities with geometrical parameters of ( $\chi = 16^\circ$ ,  $\phi = 49^\circ$ ) and ( $\chi = -16^\circ$ ,  $\phi = 139^\circ$ ) characterized the shrunken elliptical polarization bases as the most robust bases.

Figure 8a,b gives 3D views of the contrast variation in different polarization bases from cell C, which was affected by a higher effect of temporal decorrelation. From the estimated polarization TomoSAR dispersion (Figure 8c), it was possible to notice that the variance of dispersion increased with respect to the case of mild or lower temporal decorrelation (in Figure 7c). For the considered point C, the most robust elliptical polarization bases were characterized by ( $\chi = 6^\circ$ ,  $\phi = 42^\circ$ ) and ( $\chi = -6^\circ$ ,  $\phi = 132^\circ$ ).

As mentioned before, the analysis of the polarization TomoSAR dispersion extended to any pixel of the study area with the selection condition mentioned in Section 5.1. For the pixels, the most robust polarization bases, through identification of the cavities, were discovered. The outcomes from the histograms of the identified polarizations in Figures 9 and 10 coincided with the previously reported results. The histograms provided detailed insight into the discovered robust polarization bases: From the means and standard deviations of the geometrical parameters (reported in the captions of Figures 9 and 10), the polarization bases with parameters of ( $\mu_\chi = 12.5^\circ$ ,  $\mu_\phi = 42^\circ$ ) and ( $\mu_\chi = -12.8^\circ$ ,  $\mu_\phi = 132^\circ$ ) were mainly recognized as the polarization bases most robust to the effect of temporal decorrelation.

The above analyses assessed the effectiveness of TomoSAR focusing with respect to temporal decorrelation in different polarization bases. This evaluation of polarization TomoSAR dispersion

(using the reported results) provided some important indications for a two-component signal from forested areas:

- (1) The left- and right-handed circular polarization bases were the polarizations most sensitive to the effect of temporal decorrelation;
- (2) The conventional horizontal–vertical polarization basis was not characterized as a basis robust to the effect of temporal decorrelation, while usually it is possible to find very shrunk elliptical or somehow linear polarization bases with orientations of around  $42^\circ$  and  $132^\circ$  as the bases most robust to temporal decorrelation;
- (3) The variance of polarization TomoSAR dispersion changed with the level of temporal decorrelation: The higher the effect of temporal decorrelation, the higher the variance of the dispersion.

## 7. Conclusions

This paper introduced a comparative practical analysis on the behavior of temporal decorrelation with respect to the employed polarization. Temporal decorrelation is recognized as one of the most major problems in the application of SAR tomography in vegetation scenarios. The main insight of this paper lies in a polarization synthesis from a multibaseline fully polarimetric dataset, which allowed for a reconstruction of the vertical reflectivity in any desired polarization basis, leading to full characterization of the target's response in multidimensional space. Such a reconstruction carried all the information needed to assess the feasibility of assessing the quality of a focused signal with respect to polarization. It was shown that the definition of polarization TomoSAR dispersion, constructed by the contrast difference between original and temporally affected reflectivity in all possible polarization bases, allowed for a comparative assessment of the sensitivity of polarization with respect to the possible effects induced by temporal decorrelation on a reconstructed vertical profile.

The analysis was performed with simulated and real data from the BioSAR 2007 ESA campaign of forested areas. In this regard, a simulation process of generating multitemporal data affected by temporal decorrelation with a peculiarity of forest height and polarization dependence was employed. The results from both the simulated and real datasets showed that temporal decorrelation had nearly the same pattern in a vegetation scenario with two-component signals, including ground and canopy contributions. The experiments verified that circular polarizations were the most sensitive polarization bases to temporal decorrelation, while a 42-degree-oriented polarization basis was characterized as the most robust polarization. It should be mentioned that apart from the amount of temporal decorrelation (mild or strong), its destructive effect showed similar behavior with respect to the polarizations. Finally, we conclude that the outcomes of the performed analyses complement frequency-oriented studies and are particularly useful for optimal data selection for feasible TomoSAR applications and for the design of new spaceborne missions based on repeat-pass processing.

**Author Contributions:** Conceptualization, methodology, validation, and implementation, H.A.; validation, conceptualization, review, and editing, G.F. and G.S.

**Funding:** The present paper was supported by University of Naples Parthenope Ricerca Competitiva 2017 (D.R. 289/2017)

**Acknowledgments:** The authors would like to thank the ESA Earth Observation Campaigns Data Project for providing MB SAR data.

**Conflicts of Interest:** The authors declare no conflicts of interest.

## References

1. Aghababae, H.; Ferraioli, G.; Schirinzi, G.; Sahebi, M.R. The Role of Nonlocal Estimation in SAR Tomographic Imaging of Volumetric Media. *IEEE Geosci. Remote Sens. Lett.* **2018**, *15*, 729–733. [[CrossRef](#)]
2. Cazcarra-Bes, V.; Tello-Alonso, M.; Fischer, R.; Heym, M.; Papathanassiou, K. Monitoring of Forest Structure Dynamics by Means of L-Band SAR Tomography. *Remote Sens.* **2017**, *9*, 1229. [[CrossRef](#)]

3. Del Campo, G.M.; Shkvarko, Y.; Reigber, A.; Nannini, M. TomoSAR Imaging for the Study of Forested Areas: A Virtual Adaptive Beamforming Approach. *Remote Sens.* **2018**, *10*, 1822. [CrossRef]
4. Tebaldini, S.; Rocca, F. Multibaseline Polarimetric SAR Tomography of a Boreal Forest at P- and L-Bands. *IEEE Trans. Geosci. Remote Sens.* **2012**, *50*, 232–246. [CrossRef]
5. Nasa-isro Sar Mission. Available online: <https://nisar.jpl.nasa.gov/> (accessed on 15 December 2018).
6. Tandem\_1 mission. Available online: <https://www.tandem-l.de/> (accessed on 15 December 2018).
7. Aghababae, H.; Budillon, A.; Ferraioli, G.; Pascazio, V.; Schirinzi, G. Assessment of temporal decorrelation in differential sar tomography for forestry applications. In Proceedings of the 12th European Conference on Synthetic Aperture Radar, Aachen, Germany, 4–7 June 2018; pp. 1–5.
8. Lombardini, F.; Cai, F. Temporal decorrelation-robust sar tomography. *IEEE Trans. Geosci. Remote Sens.* **2014**, *52*, 5412–5421. [CrossRef]
9. Minh, D.H.T.; Tebaldini, S.; Rocca, F.; Toan, T.L. The impact of temporal decorrelation on biomass tomography of tropical forests. *IEEE Trans. Geosci. Remote Sens. Lett.* **2015**, *12*, 1297–1301. [CrossRef]
10. Jung, J.; Kim, D.; Laval, M.; Yun, S. Coherent change detection using insar temporal decorrelation model: A case study for volcanic ash detection. *IEEE Trans. Geosci. Remote Sens.* **2016**, *54*, 5765–5775. [CrossRef]
11. Lombardini, F.; Griffiths, H.D. Effect of temporal decorrelation on 3d sar imaging using multiple pass beamforming. In Proceedings of the EUREL—IEEE Radar and Sonar Signal Processing, Peebles, UK, 5–8 July 1998.
12. Rocca, F. Modeling interferogram stacks. *IEEE Trans. Geosci. Remote Sens.* **2007**, *45*, 3289–3299. [CrossRef]
13. Morishita, Y.; Hanssen, R.F. Temporal decorrelation in l-, c-, and x-band satellite radar interferometry for pasture on drained peat soils. *IEEE Trans. Geosci. Remote Sens.* **2015**, *53*, 1096–1104. [CrossRef]
14. Joerg, H.; Pardini, M.; Hajnsek, I.; Papathanassiou, K.P. First multi-frequency investigation of sar tomography for vertical structure of agricultural crops. In Proceedings of the EUSAR 2014; 10th European Conference on Synthetic Aperture Radar, Berlin, Germany, 3–5 June 2014; pp. 1–4.
15. Pardini, M.; Papathanassiou, K.P. Tomosar vertical profiles at multiple sar frequencies: An experimental analysis. In Proceedings of the 12th European Conference on Synthetic Aperture Radar, Aachen, Germany, 4–7 June 2018; pp. 1–3.
16. Fornaro, G.; Serafino, F.; Soldovieri, F. Three-dimensional focusing with multipass sar data. *IEEE Trans. Geosci. Remote Sens.* **2003**, *41*, 507–517. [CrossRef]
17. Huang, Y.; Ferro-Famil, L.; Reigber, A. Under-foilage object imaging using sar tomography and polarimetric spectral estimators. *IEEE Trans. Geosci. Remote Sens.* **2012**, *50*, 2213–2225. [CrossRef]
18. Sauer, S.; Ferro-Famil, L.; Reigber, A.; Pottier, E. Three-dimensional imaging and scattering mechanism estimation over urban scenes using dual-baseline polarimetric insar observations at l-band. *IEEE Trans. Geosci. Remote Sens.* **2011**, *49*, 4616–4629. [CrossRef]
19. Zyl, J.J.V.; Zebker, H.A.; Elachi, C. Imaging radar polarization signatures: Theory and observation. *Radio Sci.* **1987**, *22*, 529–543.
20. Tragl, K. Polarimetric radar backscattering from reciprocal random targets. *IEEE Trans. Geosci. Remote Sens.* **1990**, *28*, 856–864. [CrossRef]
21. Aghababae, H.; Fornaro, G.; Schirinzi, G. Phase calibration based on phase derivative constrained optimization in multibaseline sar tomography. *IEEE Trans. Geosci. Remote Sens.* **2018**, *56*, 6779–6791. [CrossRef]
22. Laval, M.; Simard, M.; Hensley, S. A temporal decorrelation model for polarimetric radar interferometers. *IEEE Trans. Geosci. Remote Sens.* **2012**, *50*, 2880–2888. [CrossRef]
23. Arii, M.; Zyl, J.J.V.; Kim, Y. Adaptive model-based decomposition of polarimetric sar covariance matrices. *IEEE Trans. Geosci. Remote Sens.* **2011**, *49*, 1104–1113. [CrossRef]
24. Hajnsek, I.; Scheiber, R.; Ulander, L.; Gustavsson, A.; Sandberg, G.; Tebaldini, S.; Guarnieri, A.M.; Rocca, F.; Bombardini, F.; Pardini, M. Biosar 2007 Technical Assistance for the Development of Airborne Sar and Geophysical Measurements during the Biosar 2007 Experiment: Final Report without Synthesis. *ESA Contract*. 2008. Available online: <https://elib.dlr.de/5992/> (accessed on 1 October 2018).

